

# Dissociative ionization and Coulomb explosion of CH<sub>3</sub>I in intense femto second laser fields<sup>★</sup>

Dongdong Zhang<sup>1</sup>, Sizuo Luo<sup>1</sup>, Haifeng Xu<sup>1</sup>, Mingxing Jin<sup>1</sup>, Fuchun Liu<sup>1</sup>, Bing Yan<sup>1</sup>, Zhigang Wang<sup>1</sup>, Hang Liu<sup>1</sup>, Dianwu Jiang<sup>1</sup>, André Eppink<sup>2</sup>, Wim Roeterdink<sup>3</sup>, Steven Stolte<sup>1,4,5,a</sup>, and Dajun Ding<sup>1</sup>

<sup>1</sup> Institute of Atomic and Molecular Physics, Jilin University, Qianjin Avenue 2699, Changchun 130012, P.R. China

<sup>2</sup> Institute for Molecules and Materials, Radboud Universiteit Nijmegen, Heijendaalseweg 135, 6525 AJ Nijmegen, The Netherlands

<sup>3</sup> HIMS, Faculty of Science, Mathematics and Informatics, University of Amsterdam, Science Park 904, 1090 GD Amsterdam, The Netherlands

<sup>4</sup> Dept. of Physics and Astronomy, LaseRLaB, Vrije Universiteit Amsterdam, De Boelelaan 1081, 1081HV Amsterdam, The Netherlands

<sup>5</sup> CEA-Saclay, IRAMIS/LIDYL, Bât. 462, 91191 Gif-sur-Yvette Cedex, France

Received 13 January 2017

Published online 13 June 2017

© The Author(s) 2017. This article is published with open access at [Springerlink.com](http://Springerlink.com)

**Abstract.** The interaction of CH<sub>3</sub>I molecules with 100 fs 800 nm linearly polarized laser fields has been investigated at the intensity region from  $2.6 \times 10^{14}$  to  $5.8 \times 10^{14}$  W/cm<sup>2</sup> by means of a velocity map imaging method. The kinetic energy distribution of the various atomic fragment ions I<sup>q+</sup> ( $q = 1-3$ ) has been measured and reproduced by a fit of multiple Gaussian functions. Several dissociative ionization and Coulomb explosion channels were identified for I<sup>q+</sup> ( $q = 1-3$ ). As expected for a geometric alignment dominated interaction process the anisotropic angular recoil distributions of the atomic ion fragments are peaked in the laser polarization direction. The kinetic energy release (KER) of I<sup>q+</sup> ( $q = 1-3$ ) depending upon the laser intensity has been investigated. The relative weight of the various contributions from the identified dissociative ionization (DI) and Coulomb explosion (CE) channels is found to depend strongly on the laser intensity.

## 1 Introduction

The interaction of strong laser fields with molecules, about 2 decade's an active area of research already, forms a subject of exploration up till the present [1–14]. When the intensity of a laser beam approaches around  $10^{14}$  W/cm<sup>2</sup>, the strength of its electric field is comparable to that experienced by the molecular valence electrons. This gives rise to interesting phenomena, such as multi photon ionization (MPI), dissociative ionization (DI) [1–4], field ionization [5,8], Coulomb explosion (CE) [6,7,9–11], field assisted dissociation and electron re-scattering [12–14]. It is a challenging task to unify the mechanism that lead to these phenomena. The CE of a molecule is one of the most studied mechanisms. CE leads to the generation of (multiple) positively charged ionic fragments. Typically, the kinetic energy disposed into a CE fragment ion turns out to be substantially less than that expected for a prompt dissociative ionization of a parent molecule at

its equilibrium bond length  $R_E$ . It was inferred that CE occurs at a larger critical bond length  $R_C$  due to bond softening induced by the laser field [10,15,16]. Various models have been developed to explain this reduction in Coulomb energy, for example, the two-step model [10], the Thomas-Fermi-Dirac (TFD) model [17], the charge transfer enhanced ionization (CREI) model [15,16,18–21] and the Molecular Ammosov-Delone-Krainov (MO-ADK) model [22–24]. The temporal rise of the  $E$ -field amplitude laser pulse brings about a weakening of the binding energy of the valence electrons to the molecules. Consequently, the molecular bond length increases from its  $R_E$  until the laser pulse reaches its maximum intensity at which the laser pulse brings about a weakening of the binding energy of the valence electrons to the molecules. Consequently, the molecular bond length increases from its  $R_E$  until the laser pulse reaches its maximum intensity at which the bond length stabilizes at its critical length  $R_C$ . Consequently, the molecule ionizes predominantly at  $R \approx R_C$ . The fragment ions born out of such a CE usually give rise to an anisotropic angular distribution which favors the direction of the polarization vector of the laser field [18,25–34]. Such anisotropic angular distributions are

<sup>★</sup> Contribution to the Topical Issue: “Dynamics of Molecular Systems (MOLEC 2016)”, edited by Alberto Garcia-Vela, Luis Banares and Maria Luisa Senent.

<sup>a</sup> e-mail: [stolte@chem.vu.nl](mailto:stolte@chem.vu.nl)

characteristic for a CE based on a dynamic or a geometric alignment mechanism or on a combination of these two.

In the dynamic alignment mechanism it is the  $E$ -field amplitude of the laser pulse, which during its rising slope induces a dipole, reflecting the anisotropic polarizability of the parent molecule. The interaction between this induced dipole moment and the  $E$ -field amplitude of the laser field pre-aligns the parent molecular axis to the laser's  $E$ -field amplitude until the molecular bond stabilizes. Subsequently a Coulomb Explosion occurs after which the ionic fragments recoil direction is parallel to the  $E$ -field amplitude of the laser pulse [18,25–29].

In the geometric alignment mechanism, the anisotropic ion fragment recoil distribution reflects an extended bond ionization rate, which depends on the angle between the molecular bond axis and the polarization vector of the laser field. An additional mechanism, which could influence the recoil direction of the positive charged fragments of the Coulomb explode molecule is the Post Ionization Alignment (PIA) effect, which enhances the alignment upon the ionization of the molecule [22–24].

Methyl iodide  $\text{CH}_3\text{I}$ , a polar molecule with  $C_{3v}$  symmetry, serves as a benchmark symmetric top molecule, which has been the object of many studies. As such it served in a series of velocity map ion imaging experiments that explored the pulsed  $ns$  laser induced photo dissociation dynamics of a  $C_{3v}$  parent molecule [32–35]. The spatial alignment of  $\text{CH}_3\text{I}$  due to its exposure to intense nanosecond and picosecond pulse laser fields has been determined by the analysis of the angular recoil distribution of the photo fragments using velocity mapped ion imaging (VMI) or time of flight (TOF) mass spectrometric techniques [36–38].

The first experiment, in which the angular distribution of the ionic fragments arising from the CE of a  $\text{CH}_3\text{I}$  molecule was observed, a  $10^{16}$   $\text{W}/\text{cm}^2$ , 50 fs, 790 nm pulsed laser field was applied. As a means to observe the angular recoil distribution of the ionic fragments, Graham et al. [39] varied the direction of the laser polarization vector with respect to the axis of their time of flight mass spectrometer (TOF-MS). All angular recoil distributions of single and multiple charged fragments, detected up to  $\text{I}^{7+}$ , favored the direction of the polarization vector. Because of the shortness of the 50 fs laser pulse compared to the inverse of the rotational constant ( $1/B = 133$  ps) of  $\text{CH}_3\text{I}$ , this preference was attributed to geometrical alignment.

Ma et al. [40] irradiated  $\text{CH}_3\text{I}$  molecules with 110 fs, 810 nm laser pulses at intensities which ranged from  $2.5$  to  $25 \times 10^{15}$   $\text{W}/\text{cm}^2$ . Employing the TOF-MS technique, they succeeded, when the laser polarization was tuned parallel to the TOF axis, to resolve a spitting between the mass peaks of the atomic ion fragments whose CE induced recoil velocity pointed towards and those away from the MCP ion detector. The resulting kinetic energy releases (KERs) increased only slightly with increasing laser intensity. Experimental tests demonstrated that geometric alignment indeed was the dominating CE mechanism for  $\text{CH}_3\text{I}$  at a 110 fs laser pulse duration.

Applying 180 fs 798 nm laser pulses mainly at  $6.6 \times 10^{14}$   $\text{W}/\text{cm}^2$ , Liu et al. [41] explored the CE and DI dynamics of  $\text{CH}_3\text{I}$  employing a reflectron time-of-flight mass spectrometer. Its superb mass resolution made it possible to resolve the KERs of fragment ions (with the same mass over charge ratio) originating from different CE and DI channels. The observed CE channels were assigned by matching the recoil energy distributions of an individually resolved  $\text{CH}_3^{p+}$  and  $\text{I}^{q+}$  ion to a particular channel  $n \equiv p + q$  with  $2 \leq n \leq 10$ . Moreover all DI and CE fragment ions distributions were well described by a Gaussian distribution and also to be insensitive of the laser intensity. For each KER channel, the inter-nuclear distance  $R = R_C$ , at which the CE takes place, was obtained by matching the maximal possible KER to the height of the Coulomb potential between the fragments at  $R = R_C$ . In this and other studies it is customary to apply the pure Coulomb field approximation:

$$KER \text{ (eV)} \approx 14.4 \times p \times q / R_C \text{ (\AA)} \quad (1)$$

$R_C \approx 3.7$   $\text{\AA}$  resulted as a typical value for  $\text{CH}_3\text{I}$  independent on  $p$  and  $q$  [42]. The KER's obtained in this study refer to a geometric alignment, where the laser polarization vector pointed along the TOF axis.

In a subsequent study Wang et al. [42] applied the Velocity Mapped Ion imaging (VMI) method to explore the recoil of the ionic fragments resulting from the exposure of  $\text{CH}_3\text{I}$  to a 35 fs, 800 nm laser pulse. At their lowest intensity  $5 \times 10^{13}$   $\text{W}/\text{cm}^2$ , the observed recoil velocity distributions for of  $\text{CH}_3^+$  and  $\text{I}^+$  were found to originate from 3 different DI channels. Each of these channels fitted well to a Gaussian velocity distribution. At the more intense laser field of  $6 \times 10^{14}$   $\text{W}/\text{cm}^2$  the CE channels dominated the VMI's. Their KER's were fitted by a sum of Gaussian speed distribution functions for each of the  $\text{I}^+$ ,  $\text{I}^{2+}$  and  $\text{I}^{3+}$  fragments. The KER's agreed reasonable well with those found by Liu et al. [41] earlier at the same laser intensity but with a longer 180 fs laser pulse duration [42].

More recently, Corrales et al. [43] applied a short (50 fs) and non-resonant (804 nm) laser pulse to study the CE and DI of  $\text{CH}_3\text{I}$  in the high density region of a molecular beam. This is in contrast to the other experiments described in this paper and in previous studies [39–42]. Employing, 1 to  $6 \times 10^{13}$   $\text{W}/\text{cm}^2$  laser field intensities, much lower than those applied in previous studies [25,39–42], the recoil energy distribution of the  $\text{I}^{q+}$  and  $\text{CH}_3^{p+}$  CE ion pair fragments were found to exhibit a double peak structure at recoil energies much less than those observed in previous studies. Multiple peak structured CE recoil distributions turned out to occur for all  $q \leq 2$  CE born  $\text{I}^{q+}$  ion fragment channels. Corrales et al. [43] rationalized this novel phenomenon by the introduction of a new theoretical model. This model is based on a state-of-the-art ab initio calculation of all the one-dimensional potential curves of all  $\text{CH}_3\text{I}^{2+}$ ,  $\text{CH}_3\text{I}^{3+}$  and  $\text{CH}_3\text{I}^{4+}$  electronic dissociative and bound states that adiabatically connect to the range of electronic states of the  $\text{I}^{q+}$  ion fragment. Thereafter, assuming a vertical Franck Condon transition from the minimum of the electronic

ground state PES, the kinetic energy for each of the ionic fragment channels was evaluated propagating the neutral ground state wave packet on each of the  $\text{CH}_3\text{I}^{n+}$  potential curves. The KER of an outgoing  $\text{I}^{q+}$  CE ionic fragment was found to reflect the internal energy of the specific electronic states.

In the present paper we report a molecular beam experiment, in which the  $\text{CH}_3\text{I}$  molecules are exposed to a 100 fs, 800 nm laser field at intensities ranging from  $2.6 \times 10^{14}$  W/cm<sup>2</sup> to  $5.8 \times 10^{14}$  W/cm<sup>2</sup>. The resulting angular recoil energy distributions of the generated  $\text{I}^+$ ,  $\text{I}^{2+}$  and  $\text{I}^{3+}$  ion fragments were obtained with the VMI technique [44]. The laser intensity and recoil energy dependent branching between the various via multi photon absorption populated DI and CE explosion channels as well as their associated angular distributions of the generated iodine ions will be discussed.

## 2 Experimental setup

Our experiments were performed using a standard velocity map imaging system similar to that of Eppink and Parker [44]. At a backing pressure of 4 bar a mixture of 10%  $\text{CH}_3\text{I}$  seeded in He was expanded supersonically via a pulsed valve (General Valve Series 9, 0.5 mm orifice) into the source chamber. Before entering the ionization chamber the supersonic molecular beam was passed through a 0.5 mm  $\varnothing$  skimmer mounted 6 cm downstream from the nozzle exit. The distance between the nozzle exit and the interaction spot of the laser field with the  $\text{CH}_3\text{I}$  molecule beam in the ionization chamber was about 710 mm. A 4 mm  $\varnothing$  hole in the repeller plate of the coaxial VMI lens assembly collimated the  $\text{CH}_3\text{I}$  beam which 8 mm further downstream in the horizontal plane crossed the about  $w_0 \approx 100$   $\mu\text{m}$  waist radius of an intensive 800 nm 100 fs laser beam pulse, provided by a 10 Hz repetition rate chirped-pulse amplified Ti:sapphire Spectra Physics laser system. The total of 50–100  $\text{I}^{q+}$  ions from a Gaussian laser beam volume of  $(\pi w_0^2)^2/\lambda = 0.1233$  mm<sup>3</sup> at a density of  $(4.05\text{--}8.11) \times 10^6$   $\text{I}^{q+}$  ions/cm<sup>3</sup> generated in a single laser shot warranted that the influence of space charge onto the ion imaging process could be ignored.

Moreover the coaxial geometry of our imaging system and  $\text{CH}_3\text{I}$  beam enhanced the energy resolution of our VMI imaging system. The differentially pumped ionization chamber equipped with two turbo molecular pumps maintained a background pressure of  $5 \times 10^{-7}$  Pa at the ionization/detection chamber. A variable positive voltage  $V_R$  could be applied onto the repeller plate of our VMI system. The ions generated by the laser pulse pass through a 20 mm diameter aperture in the extractor plate, which is at a voltage of  $V_E$  ( $<V_R$ ) at a distance of 15 mm from the repeller plate. Equidistant circular concentric 1 mm tick copper plate electrodes (similar to the extractor plate) provided an approximately 198 mm long immersion ion lens system in which the fragment ions are accelerated to a kinetic energy of about  $q \cdot V_R$ . Subsequently these ions enter a 54 cm long TOF tube upon which they finally impinge onto a position sensitive detector. This detector is

equipped with dual MCPs (40 mm in diameter) coupled to a fast phosphor screen (P47).

To allow the mass selection of a particular photo-fragment ion, the gain of the MCP was gated by applying a timed 1  $\mu\text{s}$  voltage pulse (DEL, PVX-4130,  $\pm 6$  kV pulse generator) on the MCP plate, which faces a phosphor screen. All static electric fields of the ion optics were carefully adjusted to attain the velocity mapping condition. Optimal velocity mapping was obtained with  $V_E/V_R \approx 0.75$  ( $V_R = 4150$  V). Images of the signal on the phosphor screen were recorded using a CCD camera (ANDOR iKon-M) and accumulated typically for 6000–12000 laser shots. The raw images were processed using Abel inversion to obtain three-dimensional distributions of the positively charged photo-fragments.

The flight time of the various ionized molecules and fragments generated by the intensive fs laser pulse, which polarization vector is pointing parallel to the MCP plane, is proportional to their  $(m/q)^{1/2}$  ratio. To circumvent the dead time uncertainties associated to the timing of an electronically generated trigger pulse a noninvasive method has been applied to determine the  $\tau = 0$  TOF moment at which the  $\text{CH}_3\text{I}$  beam is exposed to the high intensity fs laser pulse, which causes the  $\text{CH}_3\text{I}$  molecules to Coulomb explode or to dissociative ionize into positively charged fragments. Delayed by their  $(m/q)^{1/2}$  proportional flight times an ion peak is generated at the output of the non-gated MCP detector. Where after the flight times of these peaks with respect to an unknown  $\tau = 0$  moment are registered. Next the optimal VMI  $V_E/V_R \approx 0.75$  ( $V_R = 4150$  V) repeller and extractor plate voltages were raised with a factor of 2. This raise implies that all mass peaks shorten their flight time  $\tau$  with a factor  $\sqrt{2}$  compared to their flight time at the optimal VMI condition. The MCP arrival times obtained are plotted as a function of the  $(m/q)^{1/2}$  value of all identified ion mass peaks. This plot results in 2 lines, which differ a factor *surd2* in slope and cross at the  $(m/q)^{1/2} = 0$  ordinate axis position, which denotes the sought after  $\tau = 0$  laser pulse firing moment. The precondition that the laser polarization vector has to point parallel to the MCP precludes a TOF peak split of a CE and MI produced ion fragment observed at some of the previous studies [37,41] and validates that at a VMI condition  $\tau = L_{eff} \sqrt{\frac{2m}{q \cdot V_s}}$ . Where  $L_{eff}$  denotes the effective length of a TOF tube. Hence

$$v = L_{eff}/\tau = \sqrt{(q \cdot V_s)/2m}. \quad (2)$$

The empirical relation between the velocity component of  $\nu$  along the TOF axis of a CE or DI resulting in the  $\text{CH}_3\text{I}$  ion fragment transversal recoil velocity vector  $\vec{u}'$  points perpendicular to TOF axis, and the VMI will be positioned on a sharply intensified circle with radius:

$$R = N \cdot u' \cdot \tau \quad (3)$$

where  $N$  denotes the amplification factor in  $R = N \cdot L_{eff}$  [44]. The  $N$  value of our apparatus, needed to calibrate the  $\text{I}^{q+}$  recoil velocities, was obtained numerically (SIMION 6.0).

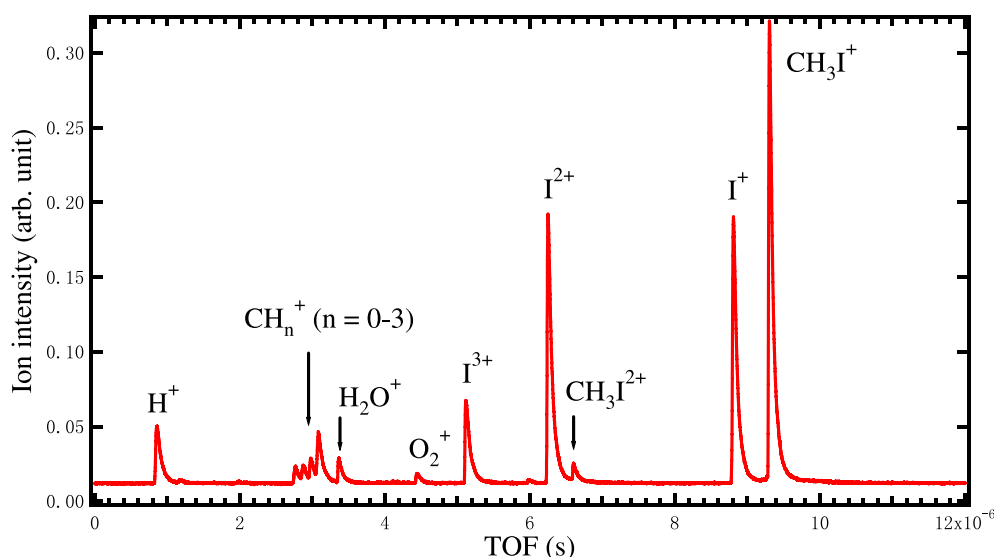


Fig. 1. TOF mass spectra of  $\text{CH}_3\text{I}$  irradiated by 800 nm, 100 fs laser pulses at intensities of  $3.8 \times 10^{14} \text{ W/cm}^2$ .

### 3 Results and discussion

#### 3.1 Time-of-flight mass spectra

Figure 1 shows a typical TOF mass spectrum of  $\text{CH}_3\text{I}$  molecules after interaction with an 800 nm 100 fs laser pulse at an intensity of  $3.7 \times 10^{14} \text{ W/cm}^2$  obtained at the optimal velocity mapping  $V_E$  and  $V_R$  voltages. The dominant peaks in the mass spectrum are the  $\text{CH}_3\text{I}^{n+}$  ( $n = 1-2$ ) parent ions, the fragment  $\text{CH}_k^+$  ( $k = 0-3$ ) group and the fragment iodine ions,  $\text{I}^{q+}$  ( $q = 1-3$ ). The presence of the multiple charged fragment ions indicates that a Coulomb explosion (CE) process in the intense laser field is taking place. These ions are produced in quantities that are comparable to those of singly charged iodine ions, which indicates a competition between Coulomb explosion and multi-photon dissociative ionization (MPDI) channels. The small mass peak, which corresponds with the double charged  $\text{CH}_3\text{I}^{2+}$  parent ion, is clearly resolved in the TOF spectrum. The observation of a double charged parent ion indicates the presence of a well in the Potential Energy Surface (PES) along the C-I bond reaction coordinate which is deep enough to permit a stable  $\text{CH}_3\text{I}^{2+}$  ion [41,43]. Similar phenomena and corresponding calculations have been reported about the CE process of  $\text{N}_2$  and  $\text{O}_2$  in an intense laser field [24,43]. As to be expected the longer the laser pulse lasts at a particular laser intensity the more fragmentation of the  $\text{CH}_3^+$  radical ions is observed. Raising the laser intensity at fixed pulse duration renders the same effect. Since the maximal  $5.8 \times 10^{14} \text{ W/cm}^2$  laser intensity, applied in the present experiment, is almost two order magnitude larger than the maximal laser intensity in the Corrales et al. [43] experiment, the number of observed  $\text{CH}_3\text{I}$  KER ( $p, q$ ) channels in the present study is appreciably larger. There is no indication of  $\text{CH}_3\text{I}$  cluster formation in the TOF mass spectrum, probably due to the low  $\text{CH}_3\text{I}$  (X) concentration in the gas mixture at the expansion stage.

To investigate the nature of the well of the  $\text{CH}_3\text{I}^{2+}$  precursor ion C-I bond at our laser intensities, ab initio computations employing the Molpro2010 package have been carried out. The 46 inner electrons of the iodine atom, were accounted for by a relativistic effective core potential and the valence  $5s5p$  electron were described with a contracted Gaussian basis set ( $9s9p3d2f1g$ )/[ $5s5p3d2f2g$ ]. To account for the interactions involving the carbon and/or the hydrogen atoms, an all-electron Gaussian basis set aug-cc-pVTZ was used. The state-average complete active space self-consistent field (SA-CASSCF) method was utilized to generate optimized zero-order wave functions. To account for dynamic correlations multistate-CAS second-order perturbation calculations (MS-CASPT2) were included. In the SA-CASSCF computational method, the resulting active C-I bond space consists of one bonding, one anti-bonding and two non-bonding orbitals. The spin-orbit coupling was treated at the CASSCF level, while the diagonal elements of spin-orbital matrix were replaced by the MS-CASPT2 energies of the S-states of  $\text{CH}_3\text{I}^{2+}$ . These calculations yielded the electronic ground states of the  $\text{CH}_3\text{I}$  neutral, which 2.3 eV well depth is in accordance with experimental results [33] and the well depths of the  $\text{CH}_3\text{I}^{n+}$  ions with  $n$  up to 3. The geometry of  $\text{CH}_3$  radical was assumed to remain fixed at these one dimensional PES's of the  $\text{CH}_3\text{I}^{n+}$  ( $n = 0, 1, 2, 3$ ) electronic ground state. The  $n \leq 3$  predicted well depths are consistent with a well deep enough for a bound  $\text{CH}_3\text{I}^{3+}$  ion with respect to its C-I bond breaking stretch coordinate. Spectroscopic determined C-I bond length dependence of the various dissociative channels of the  $\text{CH}_3\text{I}^+$  ion offers a convincing experimental basis for the importance of the  $\text{CH}_3\text{I}^+ \rightarrow \text{CH}_3 + \text{I}^+$  DI channel [45].

The hydrocarbon ions,  $\text{CH}_k^+$  with  $k = 0-3$  contribute also to the TOF spectrum. Unfortunately these TOF peaks overlap strongly that a measurement of a separate ion image for each of these individual ionic fragments turned out to be impossible. Moreover, the kinetic

energy of the  $\text{CH}_k^+$  fragments born out a CE process is expected to be mostly too large to impinge onto our 4 cm  $\varnothing$  MCP detector. Therefore at all our three laser intensities only the recoil velocity distributions of the slower single, double and triple charged iodine fragments could be imaged in our experiment. The observed  $\text{I}^{q+}$  fragment ion images provided both the kinetic energy and angular recoil distributions, which offered the possibility to obtain a more profound knowledge about the MPDI and CE processes that occur in  $\text{CH}_3\text{I}$  molecules that are exposed to  $2.6\text{--}5.8 \times 10^{14}$  W/cm<sup>2</sup> laser field intensities.

### 3.2 The Coulomb explosion and multi photon dissociative ionization of $\text{CH}_3\text{I}$

In a laser field, the molecular ionization process is much faster than that of dissociation. Consequently, the ionization process of a neutral  $\text{CH}_3\text{I}$  molecule takes appreciable less time than that required for the dissociation into neutral fragments. So the  $\text{CH}_3\text{I}$  molecules are first ionized by a fs pulsed laser field where after the resulting parent ion  $\text{CH}_3\text{I}^{m+}$  will dissociate into different fragment ions. When  $\text{CH}_3\text{I}^{m+}$  is irradiated by a 50 fs 804 nm  $I = 10^{13}$  W/cm<sup>2</sup> laser field MPDI is allowed [14]. When the laser intensity increases, highly charged ions are induced by the intense laser field, leading to Coulomb explosion. In an intense laser field, CE typically occurs at laser intensities of the field-induced ionization (FI) region. The probability of FI is marked by the value of the adiabatic parameter,  $AP$ , as was introduced for atoms by Keldysh [46],

$$AP = \sqrt{\frac{IE}{1.87 \times 10^{-13} \times I_0 \times \lambda^2}} \quad (4)$$

here,  $IE$  is the molecular ionization energy (in eV) in the absence of a laser field,  $I_0$  is the peak intensity of laser (in W/cm<sup>2</sup>) and  $\lambda$  is the laser wavelength (in  $\mu\text{m}$ ). Generally, values of  $AP < 1$  indicate participation of the FI mechanism, while values of  $AP > 1$  imply that the MPI mechanism is dominant. In the present case of  $\text{CH}_3\text{I}$  ( $IE = 9.54$  eV) and  $\lambda = 800$  nm, according to equation (3) the ( $AP = 1$ ) turning point occurs at  $I_0 = 7.9 \times 10^{13}$  W/cm<sup>2</sup>. Since  $I_0$  denotes the laser beam axis intensity maximum of the Gaussian shaped intensity beam profile and because the laser intensity range applied in the present study ranges from  $2.6 \times 10^{14}$  W/cm<sup>2</sup> to  $5.8 \times 10^{14}$  W/cm<sup>2</sup>, one expects significant contributions both from the CE and the DI ionization channels. These channels are labeled  $G_q(p, q)$ , where  $p \geq 0$  and  $q \geq 0$  denote respectively the charge numbers of the  $\text{CH}_3^{p+}$  and the  $\text{I}^{q+}$  fragments. The eventual presence of an additional channel at a particular  $q$  is indicated as  $G_q(p, q')$ . The specifics observed for the  $G_1(0, 1)$ ,  $G_1(0, 1')$  and  $G_2(0, 2)$ ,  $P(E_t)$  multi photon DI channels are given in Sections 3.3 and 3.4.

### 3.3 The $\text{I}^+$ , $\text{I}^{2+}$ and $\text{I}^{3+}$ ion fragment recoil energy distributions at a laser intensity of $3.7 \times 10^{14}$ W/cm<sup>2</sup>

The most left panels of Figure 2 depict the raw VMI images of  $\text{I}^+$ ,  $\text{I}^{2+}$ , and  $\text{I}^{3+}$  fragment ions obtained at a laser intensity of  $3.8 \times 10^{14}$  W/cm<sup>2</sup>. The polarization vector of the laser pointed along the vertical direction of the image plane. As expected an  $\text{I}^{q+}$  ion favors to recoil along the polarization vector of our intense fs laser field. The VMI images of the  $\text{CH}_3\text{I}^+$  and  $\text{CH}_3\text{I}^{2+}$  parent ions correspond to a tiny spot at the center of the phosphor screen. These isotropic spots are not displayed in Figure 2. The central column of Figure 2 displays the ion images that result from enforcing the raw ion images left-right and top-down symmetry with respect to the horizontal and vertical line of the ion images. Moreover an ideal ion image is expected to be symmetric with respect to the vertical axis, which is assumed also to cross the image position of the parent ion. The minute disturbances to a perfect four-fold symmetry of the raw ion images are due to image errors which originate from imperfect ion optics, from an imperfect alignment of the polarization vector along the vertical direction and/or from an imperfect homogenous gain over the surface of the dual MCP. In the present experiment much care was taken to align the polarization vector of the intense laser field along the vertical direction, which resulted in a nearly fourfold symmetric ion image. All observed ion images, shown in the left column of Figure 2 are almost identical to the four-fold symmetrical ones in the central column. The panels in the right column of Figure 2 display the Abel inverted cylindrical symmetric recoil velocity distribution of the  $\text{I}^{q+}$  fragments with respect to the polarization vector, as obtained with the ‘‘Davis62’’ computer code [47].

Upon the integration over the full range of recoil angles of the cylinder symmetric reconstructed 3D velocity mapped ion images, the recoil velocity distribution for each of the three differently charged iodine ions is obtained. Subsequently, these velocity distributions were converted to kinetic energy recoil (KER) distribution which include the contribution of the non-observed  $\text{CH}_3^{p+}$  fragment. The KER (also called  $E_t$ ) in the center of mass system follows from:

$$KER = \frac{m_{\text{CH}_3\text{I}}}{m_{\text{CH}_3}} \times KER_I = 9.47 \times KER_I \quad (5)$$

in which  $KER_I$  corresponds to the CMS kinetic energy release of solely the  $\text{I}^{q+}$  ( $q = 1\text{--}3$ ) ion. The resulting  $P(E_t)$   $KER_I$  probability distributions, obtained from Abel inverted  $\text{I}^+$ ,  $\text{I}^{2+}$ , and  $\text{I}^{3+}$  fragment ions VMI's, are shown in Figure 3. For each of the three  $P(E_t)$  distributions the recoil energy with the highest probability was scaled to unity. Figure 3 shows clearly that the  $P(E_t)$  distributions are distinctive for differently charged iodine ions. As the charge of the iodine fragment increases, the width of the  $P(E_t)$  distribution as well as the maximum kinetic recoil energy increases. In addition, the  $P(E_t)$  distribution of the  $\text{I}^+$  fragment carries two distinctive recoil features, one at low kinetic energy (centered at about 0.1 eV) and one

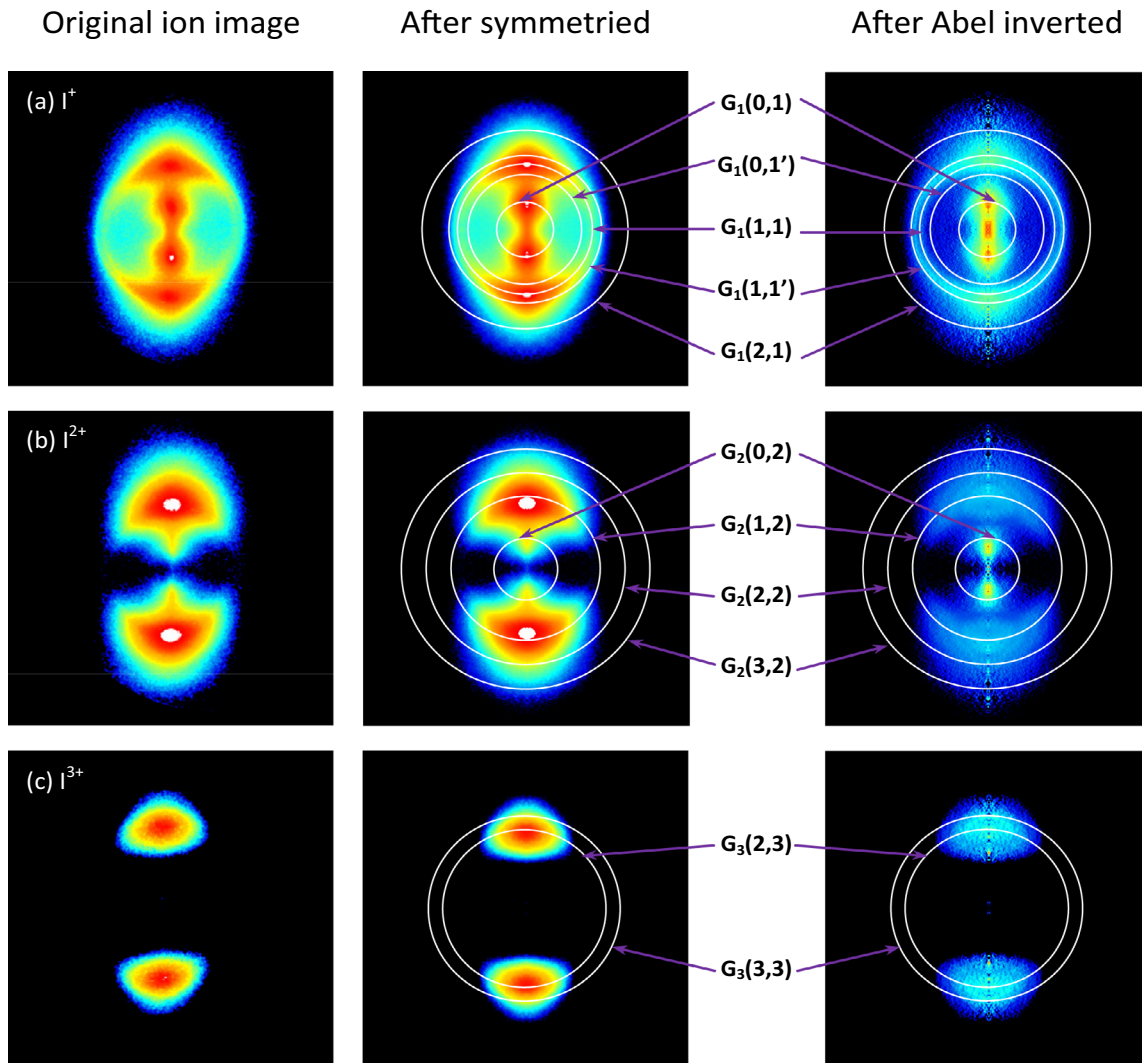


**Fig. 2.** Images of  $I^+$ ,  $I^{2+}$  and  $I^{3+}$  at laser intensity of  $3.7 \times 10^{14}$  W/cm<sup>2</sup>. The white circles in (a–c) label the peak position of the kinetic energy components. Each kinetic energy component is labeled by  $G_q(p, q)$ . The capital letter G means that we use Gaussian function as the fitting function. The numbers  $p$  and  $q$  are defined as  $\text{CH}_3\text{I}^{(p+q)+} \rightarrow \text{CH}_3^{p+} + \text{I}^{q+}$ . The prime symbol ' after the  $q$  denotes an additional Coulomb explosion channel.

at high kinetic energy (centered at about 0.5 eV). The  $P(E_t)$  distribution of the  $I^{2+}$  fragment exhibits a less pronounced shoulder at the low kinetic energy region. The  $P(E_t)$  distribution of the  $I^{3+}$  fragment, however, shows no evidence at all for a low kinetic energy distribution feature. Liu et al. [41] succeeded to simulate their observed TOF high-resolution mass spectra of various  $p$  and  $q$  charged ion fragments of  $\text{CH}_3\text{I}$ , in which they presumed a Gaussian shaped velocity recoil distribution for each of their  $(p, q)$  channels. In the present paper also a Gaussian translational energy  $P(E_t)$  distribution was assumed for each of the individual  $(p, q)$  DI or CE channels:

$$P(E_t) = \frac{C}{\frac{1}{2}W\sqrt{2\pi}} \exp\left[-\frac{\ln 2 \times (E_t - E_{peak})^2}{\frac{1}{2}W^2}\right] \quad (6)$$

where,  $E_{peak}$  and  $W$  are the peak value and the FWHM of the kinetic energy distribution respectively.  $C$  is a nor-

malization factor. As Figure 3 shows, the application of equation (6) leads to a nearly perfect fit for each of our  $I^q+$  recoil energy distributions. The number of DI and CE channels as well as their experimental values of  $E_{peak}$  for each of the VMI's shown in Figure 2, were based on the structured polar angle and recoil energy dependencies. The white circle radii in Figure 2 denote the peak intensity position of the kinetic energy released for each of the distinct DI and CE channels. Table 1 lists both the  $E_{peak}$  and  $W$  values of the CE channels obtained in our experiment and those of previous experiments [41–43].

Typically, for most CE channels the KER's as observed by Liu et al. [41] and also those obtained by Wang et al. [42] are somewhat larger than the ones obtained in our experiment. Partially, these differences are due to the intensity enhancement of the faster ion fragments with respect to the slower ones in a TOF experiment with respect to the  $I^q+$  VMI detected signal, which lacks this recoil

velocity biased enhancement. Additionally, in the experiment of Liu et al. [41] only the CE ion fragments that favor to recoil along the axis of the high resolution reflectron TOF Mass Spectrometer are detected, while in the present experiment this restriction is absent. Finally the 35 fs laser pulse applied in the experiment by Wang et al. [42], compared to the 100 fs pulse used in our experiment, also leads to larger KER's. This because the critical C-I bond stretch, at which the CE occurs, decreases upon shortening of the laser pulse.

The observations by Corrales et al. [43] lead to much larger KER's than those of the present and earlier observed ones [41,42]. These differences were attributed to a different type of Coulomb explosion mechanism associated to their at least an order of magnitude less intense fs laser pulses.

To obtain realistic values for  $R_C$ , it turned out to be necessary to assign only the  $E_{peak} \geq 0.4$  eV as CE channels. Consequently, the  $I^+$  and  $I^{2+}$   $E_{peak} < 0.4$  eV fragment channels are DI channels. The Gaussian  $P(E_t)$  function resulted in an excellent fit to the low  $I^+$  kinetic recoil energy range of the experimental KERs depicted in the (a) and (b) panels of Figure 3. This procedure evidenced the presence of at least two distinctive ionization channels  $G_1(0, 1)$  and  $G_1(0, 1')$ , centered at  $E_{peak} = 0.06$  eV and at  $E_{peak} = 0.17$  eV respectively. The fit of the low  $I^{2+}$  recoil energy range in Figure 3 required the contribution of a single  $G_2(0, 2)$  DI channel centered at  $E_{peak} = 0.17$  eV. Table 1 provides a comparison of the energy balance based calculated KERs which are compared with the values of  $E_{peak}$  and  $W$  that resulted from the dissociative ionization channels.

### 3.4 The $G_q(0, q)$ KER channels of the multi photon dissociative ionization of $CH_3I$

The ionization process originating from the ground state  $CH_3I(X)$  molecule is much faster than the dissociation process. It requires the absorption of seven 800 nm fs photons to emit one electron of the outer shell nonbonding orbital. The resulting intermediate  $CH_3I^+(X)$  ion is expected to reside temporally in the vibrational ground state of the  ${}^2E_{3/2}$  lower or of  ${}^2E_{1/2}$  upper spin orbit rotational manifold, which origins respectively are shifted  $76930\text{ cm}^{-1}$  and  $81979\text{ cm}^{-1}$  upwards with respect to the  $CH_3I(X)$  ground state [48]. This is expected because the rotational constants of  $CH_3I^+(X)$   $A = 5.200\text{ cm}^{-1}$  and  $B = 0.253\text{ cm}^{-1}$  are nearly the same as those of  $CH_3I(X)$   $A = 5.174\text{ cm}^{-1}$  and  $B = 0.250\text{ cm}^{-1}$  [47,49]. The large Franck Condon factor associated with these nearly similar rotational constants strongly enhances the multi photon absorption rate for this particular transition. Moreover, the  $CH_3I^+[{}^2E_{3/2}(X)]$  ion has to absorb at least three additional 800 nm photons to rise from the  $22018\text{ cm}^{-1}$  deep PES well above the dissociation limit to the  $CH_3(X^2A'') + I^+({}^3P_j)$  fragment channel of  $CH_3I^+$  its  $\tilde{A}$  state [47,48]. This dissociation process disposes the  $CH_3$  radical fragment in the vibronic ground state [50] and  $I^+({}^3P_j)$  in the  $j = 2$  electronic ground state or in

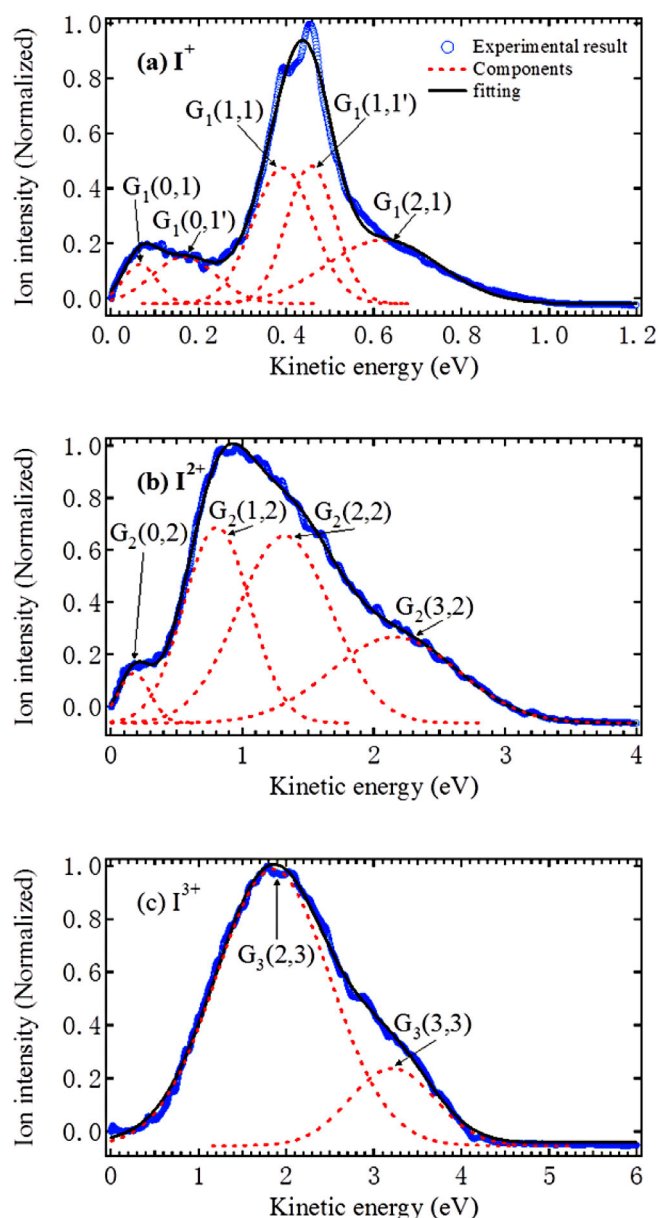


**Fig. 3.** The KER distributions of (a)  $I^+$ , (b)  $I^{2+}$ , and (c)  $I^{3+}$  fragment ion components born after laser irradiation at an intensity of  $3.7 \times 10^{14}\text{ W/cm}^2$ . In each panel, the thick blue curve is the experimental observed result, the black curve the fitting result, and the red dashed curves the KER distribution of the contributing individual channel iodine ion component that contributes to the overall  $I^+$  ion fragment KER distribution.

the  $j = 0, 1$  electronically excited states. Table 2 lists the theoretically predicted coaxial dissociation energies and KERs resulting from a three (or two) 800 nm photon absorption of a  $CH_3I^+(X, {}^2E_{3/2})$  and of  $CH_3I^+(X, {}^2E_{1/2})$  parent ion, as well our observed KERs obtained at a laser intensity of  $3.7 \times 10^{14}\text{ W/cm}^2$  for the  $j = 2$  and the  $j = 0, 1$   $CH_3(X^2A'') + I^+({}^3P_j)$  dissociation channels. For comparison also the previously determined DI KERs of  $CH_3I$

**Table 1.** The Coulomb explosion  $I^{q+}$  ( $q = 1-3$ )  $KER_I$ 's observed in this work at the particular laser intensity  $I$ , wavelength  $\lambda$  and pulse duration  $\tau$  are compared with the indicated previous studies. Note that Corrales et al. [43] applied three different laser intensities. The Coulomb explosion channels are denoted  $(p, q)$  where the  $p$  and  $q$  are defined as  $\text{CH}_3\text{I}^{(p+q)+} \rightarrow \text{CH}_3^{p+} + \text{I}^{q+}$ . If available, the value of the FWHM of that particular  $I^{q+}(p, q)$  KER peak is indicated.  $R_C$  denotes the height of the Coulomb potential that matches with the maximal probable KER of the corresponding  $(p, q)$  Coulomb explosion channel, also listed in this table. The total kinetic energy release in the center of mass system follows from:  $KER_{\text{cm}} \equiv \frac{m_{\text{CH}_3\text{I}}}{m_{\text{CH}_3}} \times KER_I = 9.47 \times KER_I$ .

| Coulomb explosion channel $(p, q)$ | This work:<br>$I = 5.8 \times 10^{14}$ W/cm <sup>2</sup><br>$\tau = 100$ fs pulse<br>$\lambda = 800$ nm |                    | Liu et al. [41]:<br>$I = 6 \times 10^{14}$ W/cm <sup>2</sup><br>$\tau = 180$ fs pulse<br>$\lambda = 798$ nm |                    | Wang et al. [42]:<br>$I = 6.6 \times 10^{14}$ W/cm <sup>2</sup><br>$\tau = 35$ fs pulse<br>$\lambda = 800$ nm |                    | Corrales et al. [43]:<br>$I = 1.0 \times 10^{13}$ W/cm <sup>2</sup><br>$\tau = 50$ fs pulse<br>$\lambda = 804$ nm |                    |
|------------------------------------|---|--------------------|---|--------------------|---|--------------------|---|--------------------|
|                                    | $KER_I(p, q)$<br>FWHM [eV]  | $R_C(p, q)$<br>[Å] | $KER_I(p, q)$<br>FWHM [eV]  | $R_C(p, q)$<br>[Å] | $KER_I(p, q)$<br>FWHM [eV]  | $R_C(p, q)$<br>[Å] | $KER_I(p, q)$<br>FWHM [eV]  | $R_C(p, q)$<br>[Å] |
| (1, 1)                             | $0.39 \pm 0.12$<br>0.13<br>FWHM   | 3.9                |   |                    |   |                    | 0.46  | 3.3                |
| (1, 1')                            | $0.43 \pm 0.12$<br>0.10<br>FWHM   | 3.5                | 0.43  | 3.5                | 0.46  | 3.3                | 0.55  | 2.8                |
| (2, 1)                             | $0.65 \pm 0.02$<br>0.32<br>FWHM   | 4.8                | 0.86  | 3.5                |   |                    | $I = 3.0 \times 10^{13}$ W/cm <sup>2</sup>  |                    |
| (1, 2)                             | $0.80 \pm 0.07$<br>0.46<br>FWHM   | 3.8                | 0.85  | 3.6                |   |                    | 1.06<br>0.2<br>FWHM   | 2.9                |
| (2, 2)                             | $1.32 \pm 0.04$<br>0.70<br>FWHM   | 4.6                | 1.62  | 3.8                |   |                    |   |                    |
| (3, 2)                             | $2.15 \pm 0.05$<br>1.12<br>FWHM   | 4.2                | 2.37  | 3.8                | 3.32  | 2.7                | $I = 6.0 \times 10^{13}$ W/cm <sup>2</sup>  |                    |
| (1, 3)                             |   |                    | 1.25  | 3.6                |   |                    | 1.67  | 2.7                |
| (1, 3')                            |   |                    |   |                    |   |                    | 2.34  | 1.9                |
| (2, 3)                             | $2.04 \pm 0.08$<br>1.01<br>FWHM   | 4.5                | 2.22  | 3.8                | 2.58  | 3.5                | 4.26  | 2.1                |
| (3, 3)                             | $3.21 \pm 0.05$<br>1.17<br>FWHM   | 4.3                | 3.60  | 3.8                |   |                    |   |                    |
| (4, 3)                             |   |                    | 4.91  | 3.7                | 4.63  | 3.9                |   |                    |
| (4, 4)                             |   |                    | 6.59  | 3.7                |   |                    |   |                    |

**Table 2.** The calculated  $\text{I}^+$  KERs of the  $n$  photon dissociation channels of  $\text{CH}_3\text{I}^+$  and the observed  $\text{I}^+$  KERs by Liu et al. [41], Wang et al. [42] and in this work. The widths (FWHM) of these peaks are in parenthesis.

| $G_q(p, q)$   | DI channel of $\text{CH}_3\text{I}^+$  | Dissociation energy (eV) | $n$ | Calculation     |              | This work       |                               | References      |      |
|---------------|--|--------------------------|-----|-----------------|--------------|-----------------|-------------------------------|-----------------|------|
|               |  |                          |     | Production      | $KER_I$ (eV) | Production      | $KER_I$ (eV)                  | [41]            | [42] |
| $G_1(0, 1)$   | $\text{CH}_3\text{I}^{1+}(\text{X } ^2\text{E}_{3/2}) \rightarrow \text{CH}_3(^2\text{A}'') + \text{I}^{1+}(^3\text{P}_2)$       | 1.32                     | 3   | $\text{I}^{1+}$ | 0.14         | $\text{I}^{1+}$ | $0.17 \pm 0.03$<br>FWHM(0.16) |                 | 0.16 |
| $G_1(0', 1)$  | $\text{CH}_3\text{I}^{1+}(\text{X } ^2\text{E}_{1/2}) \rightarrow \text{CH}_3(^2\text{A}'') + \text{I}^{1+}(^3\text{P}_2)$       | 0.39                     | 2   | $\text{I}^{1+}$ | 0.04         | $\text{I}^{1+}$ |                               |                 | 0.03 |
| $G_1(0, 1')$  | $\text{CH}_3\text{I}^{1+}(\text{X } ^2\text{E}_{3/2}) \rightarrow \text{CH}_3(^2\text{A}'') + \text{I}^{1+}(^3\text{P}_{1,0})$   | 0.48                     | 3   | $\text{I}^{1+}$ | 0.05         | $\text{I}^{1+}$ | $0.06 \pm 0.01$<br>FWHM(0.08) | $0.07 \pm 0.03$ |      |
| $G_1(0', 1')$ | $\text{CH}_3\text{I}^{1+}(\text{X } ^2\text{E}_{1/2}) \rightarrow \text{CH}_3(^2\text{A}'') + \text{I}^{1+}(^3\text{P}_{1,0})$   | 1.11                     | 3   | $\text{I}^{1+}$ | 0.11         | $\text{I}^{1+}$ |                               |                 | 0.09 |
| $G_2(0', 2)$  | $\text{CH}_3\text{I}^{2+}(\text{X } ^2\text{E}_{1/2}) \rightarrow \text{CH}_3(^2\text{A}'') + \text{I}^{2+}(^4\text{S}_{3/2}^0)$ | $1.7 \pm 0.1$            | 1   |                 |              | $\text{I}^{2+}$ | $0.18 \pm 0.01$<br>FWHM(0.29) |                 |      |

**Table 3.** The anisotropic parameters  $\beta_{2n}$  ( $n = 1, 2, 3$ ) from the angular distribution of the MPDI channels  $G_1(0, 1)$ ,  $G_1(0, 1')$  and  $G_2(0, 2)$ .

|                         | $\beta_2$ | $\beta_4$ | $\beta_6$ |
|-------------------------|-----------|-----------|-----------|
| $G_1(0, 1), G_1(0, 1')$ | 0.73      | 0.17      | 0.11      |
| $G_2(0, 2)$             | 0.75      | 0.25      | 0.08      |

are shown [41,42]. The energy splitting between the  $j = 0$  and  $j = 1$  is too small to be resolved in our and other experiments.

The TOF mass spectra at laser intensities ranging between  $1.0 \times 10^{13}$  W/cm<sup>2</sup> and  $6.0 \times 10^{13}$  W/cm<sup>2</sup> provided by Corrales et al. [43] exhibit a minute CH<sub>3</sub>I<sup>2+</sup> mass peak whose height increased with laser intensity. Figure 1 in the present paper depicts the TOF mass spectrum obtained at a laser intensity of  $3.8 \times 10^{14}$  W/cm<sup>2</sup> showing a small but robust CH<sub>3</sub>I<sup>2+</sup> mass peak. In the RTOF-MS spectra at  $I = 6.6 \times 10^{16}$  W/cm<sup>2</sup> an intense CH<sub>3</sub>I<sup>2+</sup> mass peak was observed by Liu et al. [41]. It was their TOF mass spectrum which provided the first evidence of a bound CH<sub>3</sub>I(X)<sup>2+</sup> dication. The existence is corroborated with an ab initio calculation which predicts a 0.5 eV deep potential energy minimum at  $R_{C-I} \approx 2.1$  Å which at large  $R_{C-I}$  distances correlates to the I<sup>+</sup>(<sup>3</sup>P<sub>2</sub>) + CH<sub>3</sub><sup>+</sup>(<sup>1</sup>A<sub>1</sub>) ion fragments. However, the SA-CASSCF adiabatic potential curves of CH<sub>3</sub>I<sup>2+</sup> depicted in Figure 3 of reference [43] that correlate with the I<sup>+</sup>(<sup>3</sup>P<sub>2</sub>) channel leading to formation of metastable states does not show a well in the PES, preventing fast photo fragmentation of the parent ion.

Panel (b) of Figure 3 shows that the CH<sub>3</sub>I<sup>2+</sup>(X) also dissociates into the CH<sub>3</sub> + I<sup>2+</sup> fragments with a Gaussian  $KER_I$  distribution with a  $KER_I = 0.2$  eV and a FWHM  $W_I = 0.3$  eV, which implies according to the KER transformation equation, see equation (4), to a  $KER = 1.9$  eV with a FWHM  $W = 2.8$  eV for the  $G_2(0, 2)$  channel.

The lowest eigen energy of the double charged I atom with respect to the I(<sup>2</sup>P<sub>3/2</sub>) neutral ground state is 29.58 eV of the I<sup>2+</sup>(5P<sup>3-4</sup>S<sub>3/2</sub><sup>0</sup>) state. In the limiting case that all DI dissociation energy would be deposited into  $KER$ , the CH<sub>3</sub>I<sup>2+</sup>(X) eigen energy would be about 1.9 eV above that of the I<sup>2+</sup>(<sup>3</sup>P<sub>2</sub>) + CH<sub>3</sub>(<sup>2</sup>A<sub>2</sub>'') observed DI channel. Noting that the C-I Bond dissociation energy of the A-X CH<sub>3</sub>I(X) 266 nm band has been experimentally determined to be  $D^0[\text{CH}_3\text{I}(\text{X}) \rightarrow \text{CH}_3(^2\text{A}_2'') + \text{I}(^2\text{P}_{3/2})] = 2.366 \pm 0.031$  eV [35], one implies that the eigen energy of the spatially separated CH<sub>3</sub>(<sup>2</sup>A<sub>2</sub>'') and I(<sup>2</sup>P<sub>3/2</sub>) ground state fragments is  $2.366 \pm 0.031$  eV above the X(0, 0, 0) ground state of CH<sub>3</sub>I [48]. The eigen state energy of I<sup>2+</sup>(5P<sup>3-4</sup>S<sub>3/2</sub><sup>0</sup>) is 29.58 eV above the I(<sup>2</sup>P<sub>3/2</sub>) state<sup>1</sup>. Thus we conclude that the CH<sub>3</sub>(<sup>2</sup>A<sub>2</sub>'') + I(<sup>2</sup>P<sub>3/2</sub>) channel lies 30.96 eV above the origin of CH<sub>3</sub>I(X) and that the origin of the CH<sub>3</sub>I<sup>2+</sup>(X) dication is 32.9 eV above the origin of CH<sub>3</sub>I(X).

<sup>1</sup> <http://physics.nist.gov/PhysRefData/Handbook/Tables/iodinetable1.htm>

### 3.5 KER and recoil angle distribution of the $G_q$ ( $p > 0, q > 0$ ) channels at a $3.7 \times 10^{14}$ W/cm<sup>2</sup> laser intensity

Typically at laser intensities above  $10^{14}$  W/cm<sup>2</sup> on the rising edge of an 800 nm laser pulse, as predicted by MO-ADK theory, a HOMO electron will escape from the molecule via tunneling ionization through the laser field lowered potential barrier of the molecular field [22]. The angle-dependent ionization probability typically mimics the shape of the outer most HOMO orbital. The loss of such an electron weakens the strength of the molecular bond, leading to a stretching of the CI bond, which maximizes at the peak of the laser  $E$ -field. There after the momentary laser field strength will drop and eventually change its sign. This allows the previously escaped electrons to scatter from the molecular ion, which on their turn excite the remaining molecule bonded electrons even more or detach them from the molecular ion. This process of rapidly increasing C-I bond length continues till the CH<sub>3</sub>I<sup>n+</sup> is stretched to the bond length at which the molecule Coulomb explodes. During this bond stretching, the component of CH<sub>3</sub>I<sup>n+</sup> its dipole polarizability tensor  $\alpha_{\perp}$  directed perpendicular to the C-I bond axis will remain essentially constant. The component parallel with the C-I axis  $\alpha_{\parallel}$ , will increase strongly with the growing length of the C-I bond. It is this mechanism, on which the so-called post-ionization alignment (PIA) effect is based [23]. Since rotational  $B$  constant of CH<sub>3</sub>I<sup>n+</sup> decreases proportionally to the square of the C-I axis  $R$  bond length, this stretching leads to a torque on the CH<sub>3</sub>I<sup>n+</sup> axis, which rotates the axis to an angle more parallel to the fs laser polarization vector, till at  $R = R_C$  the Coulomb explosion occurs. Regarding the C-I Coulomb explosion process, it is relevant to note that in the example of N<sub>2</sub> and O<sub>2</sub>, the outcome of equation (1) was found to be accurate, resulting from accurate potential energy curves of multi-charged molecular ions at inter nuclear distances larger than 3 Å [24].

At the previous CH<sub>3</sub>I CE exploring experiments, the laser pulse durations, which generated the CE of CH<sub>3</sub>I, were respectively 180 fs [41] and 35 fs [42]. Inspection of Table 1 shows that generally the  $E_{peak}$  values of the CE channels resulting from a 180 fs laser pulse exposure are larger than those from the 100 fs exposure in our experiment. Also the from 35 fs laser pulse  $E_{peak}$  values resulting are mostly larger (to a lesser extend) than those observed in our experiment. More systematic experiments are mandatory to rationalize this unforeseen trend.

Most recently Corrales et al. [43] uncovered at a Coulomb explosion mechanism in which the I<sup>q+</sup> ion fragment, born out the CE of an electronically excited CH<sub>3</sub>I molecule, instead of in its electronic ground resides in an electronically excited states which adiabatic connect to an electronically excited state of the CH<sub>3</sub>I<sup>n+</sup>CE parent ion. Their CE recoil energy distributions deviate strongly from being Gaussian. The energy splitting among the different electronic I<sup>q+</sup> ion fragment states and those among the electronic excited and ground states of their parent molecular CH<sub>3</sub>I<sup>n+</sup> ion which PES adiabatically connects

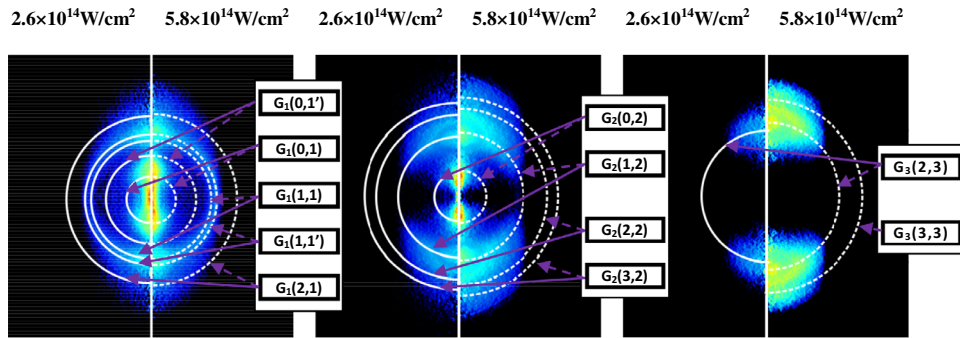


**Fig. 4.** The Abel inverted images of respectively the  $I^+$ ,  $I^{2+}$  and  $I^{3+}$  ion fragments shown in the left, center and right panel. The VMI's at the left and right side of each panel have been obtained at a laser intensity of  $I_0 = 2.6 \times 10^{14}$  W/cm<sup>2</sup> and  $I_0 = 5.8 \times 10^{14}$  W/cm<sup>2</sup> respectively. The white circles denote the most probable  $I^{q+}$  ion fragment recoil velocity of the  $G_q(p,q)$  channel.

to a particular electronic  $I^{q+}$  ion fragment state are typically dissimilar. This all implies a non-Gaussian inhomogeneous KER distribution for the VMI detected  $I^{q+}$  ion fragments.

### 3.6 The laser intensity dependence of the KER distribution of the $I^+$ , $I^{2+}$ and $I^{3+}$ ionic $CH_3I$ fragments

The VMI recoil velocity images of the  $I^+$ ,  $I^{2+}$  and  $I^{3+}$  fragment ions obtained at a laser intensity  $I_0 = 3.7 \times 10^{14}$  W/cm<sup>2</sup> have also been recorded for a lower  $I_0 = 2.6 \times 10^{14}$  W/cm<sup>2</sup> and for a higher  $I_0 = 5.8 \times 10^{14}$  W/cm<sup>2</sup> laser intensity at otherwise identical conditions. The latter Abel inverted VMI's of the  $I^+$ ,  $I^{2+}$  and  $I^{3+}$  fragment ions, were extracted from their original VMI's in a similar way as the Abel inverted VMI's of Figure 2 at  $I_0 = 3.7 \times 10^{14}$  W/cm<sup>2</sup> and are depicted for  $I_0 = 2.6 \times 10^{14}$  W/cm<sup>2</sup> in the left halve and for  $I_0 = 5.8 \times 10^{14}$  W/cm<sup>2</sup> in right halve for each of the three observed  $I^{q+}$  fragments in Figure 4. The white solid and dashed halve circles label the  $P(E_t)$  intensity maxima of the various  $G_q(p,q)$  channels which upon its individual optimized weighting factor resulted also a nearly perfect fit of the KER distribution at  $I_0 = 2.6 \times 10^{14}$  W/cm<sup>2</sup> and  $I_0 = 5.8 \times 10^{14}$  W/cm<sup>2</sup> for each of the  $I^{q+}$  ion fragments.

Assuming that this  $P(E_t)$  distribution for each of these  $G_p(p,q)$  reaction channels applied also at the lower  $I_0 = 2.6 \times 10^{14}$  W/cm<sup>2</sup> and at the upper  $I_0 = 5.8 \times 10^{14}$  W/cm<sup>2</sup> laser pulse intensities, resulted again a similar excellent fit of the observed  $I^+$ ,  $I^{2+}$  and  $I^{3+}$  KER distributions. These are shown respectively in Figure 5, panels A, B and C at  $I_0 = 2.6 \times 10^{14}$  W/cm<sup>2</sup>, at  $I_0 = 3.7 \times 10^{14}$  W/cm<sup>2</sup> and at  $I_0 = 5.8 \times 10^{14}$  W/cm<sup>2</sup> laser pulse intensities, upon employing the laser intensity optimized weighting factors for the channel depending KER distributions. As illustrated in Figure 5 and listed in Table 2, the experimental  $E_{peak}$  values of the DI channels turn out to be laser intensity independent. The experimental  $E_{peak}$  values of the CE channels shown in Table 4 increase slightly with laser intensity. This increase maximized for the CE channel

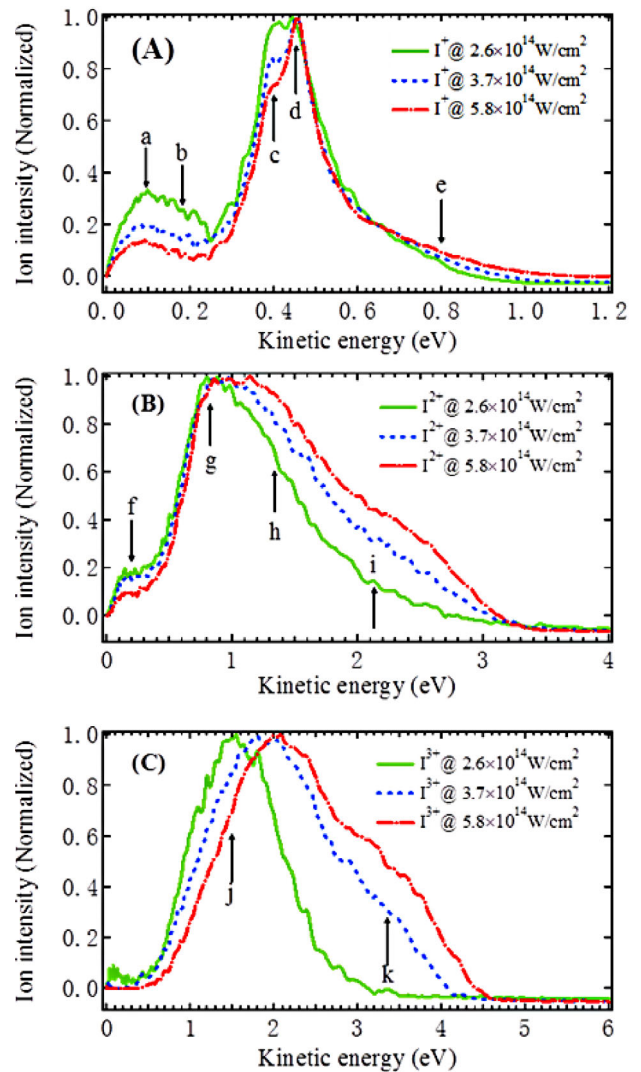


**Fig. 5.** The kinetic energy distribution of (A)  $I^+$ , (B)  $I^{2+}$ , and (C)  $I^{3+}$  fragment ions at different laser intensities. The arrows in each figure indicate different reaction channels. (a)  $G_1(0,1)$ , (b)  $G_1(0,1')$ , (c)  $G_1(1,1)$ , (d)  $G_1(1,1')$ , (e)  $G_1(2,1)$ , (f)  $G_2(0,2)$ , (g)  $G_2(1,2)$ , (h)  $G_2(2,2)$ , (i)  $G_2(3,2)$ , (j)  $G_3(2,3)$  and (k)  $G_3(3,3)$ .

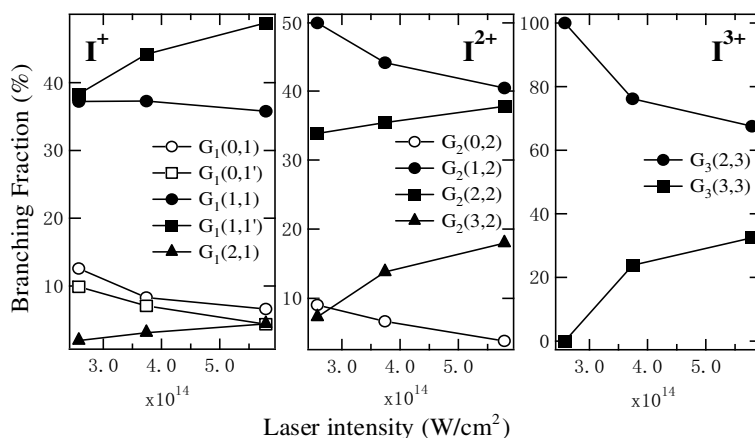


**Fig. 6.** The laser intensity dependent branching fraction of the observed DI and CE channels. The branching fraction of the particular  $I^{q+}$  ion  $G_q(p, q)$  reaction channel is equal to the intensity of that particular  $I^{q+}$  ion  $G_q(p, q)$  reaction divided by the sum of all  $G_q(p, q)$  reaction channels that contribute to the  $I^{q+}$  ion intensity.

**Table 4.** The  $KER_I$  of  $I^{n+}$  ( $n = 1-3$ ) from the various Coulomb explosion channels at different laser intensities. The Coulomb explosion channels are noted as  $(p, q)$  where the  $p$  and  $q$  are defined as  $\text{CH}_3\text{I}^{(p+q)+} \rightarrow \text{CH}_3^{p+} + \text{I}^{q+}$ .

| CE channel | Measured fragment ions | $KER_I$ (eV)                           |  |  |
|------------|------------------------|--|--|--|
|            |                        | $2.6 \times 10^{14}$ W/cm <sup>2</sup> | $3.7 \times 10^{14}$ W/cm <sup>2</sup> | $5.8 \times 10^{14}$ W/cm <sup>2</sup> |
| (1, 1)     | $I^+$                  | 0.45                                   | 0.46                                   | 0.47                                   |
| (2, 1)     | $I^+$                  | 0.70                                   | 0.72                                   | 0.75                                   |
| (1, 2)     | $I^{2+}$               | 0.78                                   | 0.80                                   | 0.84                                   |
| (2, 2)     | $I^{2+}$               | 1.22                                   | 1.32                                   | 1.43                                   |
| (3, 2)     | $I^{2+}$               | 2.01                                   | 2.15                                   | 2.22                                   |
| (2, 3)     | $I^{3+}$               | 1.85                                   | 2.04                                   | 2.21                                   |
| (3, 3)     | $I^{3+}$               |  | 3.21                                   | 3.41                                   |

with the largest  $n = p + q$  values. This we rationalize as being due to a shortening of the  $R_C$  bond length for all CE channels when one increases the laser intensity.

This all leads to an excellent fit of the kinetic recoil energy distributions for each of the  $I^{q+}$  fragments upon optimizing weight of the contributing  $G_q(p, q)$  channels at  $I_0 = 2.6 \times 10^{14}$  W/cm<sup>2</sup> and at  $I_0 = 5.8 \times 10^{14}$  W/cm<sup>2</sup> respectively. Again, similarly to those shown in Figure 3, each of the  $I^{q+}$  distributions at  $I_0 = 2.6 \times 10^{14}$  W/cm<sup>2</sup> and at  $I_0 = 5.8 \times 10^{14}$  W/cm<sup>2</sup> are normalized to  $I^{q+} = 1$  at their KER probability maximum. The normalized  $I^{q+}$  KER distributions observed at these three different  $I_0$  laser intensities are shown in Figure 5, panel (A) for  $I^+$ , panel (B) for  $I^{2+}$  and panel (C) for  $I^{3+}$ . Since all distributions were normalized to the component with the highest intensity (the  $G_1(1, 1')$  component of  $I^+$ , the  $G_2(1, 2)$  component of  $I^{2+}$ , the  $G_3(2, 3)$  component of  $I^{3+}$ ), the relative intensities of the components as a function of the laser intensity are compared to each other in Figure 6 according to their branching fraction. For the  $P(E_t)$  components at the low kinetic energy region, i.e., the  $G_1(0, 1)$ ,  $G_1(0, 1')$  and  $G_1(1, 1)$  components of  $I^+$  and the  $G_2(0, 2)$  component of  $I^{2+}$ , their relative intensity was observed to decrease for increasing laser intensity. On the other hand, the relative intensities of the components in the high kinetic energy region, the  $G_2(2, 2)$  and  $G_2(3, 2)$  components of  $I^{2+}$ , the  $G_3(3, 3)$  component of  $I^{3+}$ , increase with the laser intensity. Our results show that the outcome of the competition

between the various channels for the ionic fragmentation of  $\text{CH}_3\text{I}$  depends strongly on the intensity of the intense laser field.

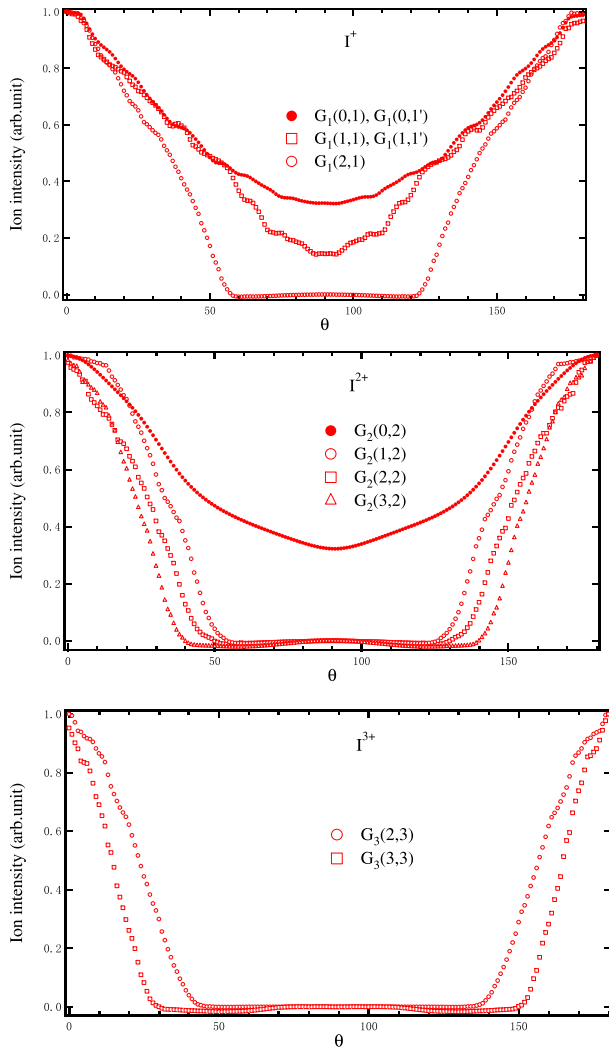
### 3.7 Angular distributions of fragment ions

Figure 7 shows the angular distributions of CE and DI  $G_q(p, q)$  channels as obtained from the Abel inverted VMI images depicted in Figure 3, taken from a narrow recoil velocity band at the  $E_t = E_{peak}$  position of  $P(E_t)$  distribution for each  $I^{q+}$  ion fragment. These angular distributions are given as a function of the angle  $\theta$  between the laser polarization axis and the fragment recoil direction, which coincides with the molecular axis.

The angular distributions of the sum of the  $G_1(0, 1)$  and  $G_1(0, 1')$  channels and that of the  $G_2(0, 2)$  DI channel have been expressed in a Legendre series:

$$I(\theta) = A \left[ 1 + \sum_{2n} \beta_{2n} P_{2n}(\cos \theta) \right]. \quad (7)$$

The significant values of the anisotropic parameters  $\beta_{2n}$  (up to  $\beta_6$ ), as obtained for each of these components, are listed in Table 5. These anisotropy parameters are a signature of the channels underlying MPDI mechanism. The duration of the 100 fs laser pulse is too short to align the  $\text{CH}_3\text{I}(X)$  parent molecule prior to MPDI with respect



**Fig. 7.** Angular distribution of fragment ions of CE and DI channels labeled with  $(p, q)$  obtained from the Abel inverted ion-images at a  $3.74 \times 10^{14}$  W/cm<sup>2</sup> laser intensity which is depicted in the most right panels of Figure 2. The ion intensity of each channel has been normalized to 1 at their maximum.  $\theta$  is the angle between the polarization direction of the laser pulse and the recoil velocity vector of the fragment ions.

to the laser polarization vector. The angular distributions of  $G_1(2, 1)$ ,  $G_2(1, 2)$ ,  $G_2(2, 2)$ ,  $G_2(3, 2)$ ,  $G_3(2, 3)$  and  $G_3(3, 3)$  CE channels are found to be strongly aligned with respect to the polarization vector of the 800 nm 100 fs laser pulse. Their ion recoil intensity drops to essentially zero over a  $60^\circ \leq \theta \leq 120^\circ$  range for  $n = 3$  up to  $30^\circ \leq \theta \leq 150^\circ$  for  $n = 6$ . Inspection of Panel (a) in Figure 2 shows the presence of a serious intensity overlap between the  $G_1(1, 1)$  and  $G_1(1, 1')$  channels. It was this recoil intensity overlap that necessitated to Abel invert the recoil angle dependency for the sum of the  $G_1(1, 1)$  and the  $G_1(1, 1')$  channels. This overlap artifact might be the reason why the recoil intensity does not drop to zero around  $\theta = 90^\circ$ .

The Coulomb explosion channels strongly favor to CE the positive charged  $I^{q+}$  and there for also the positive

charged  $\text{CH}_3^{p+}$  to recoil along the polarization vector of the intense 800 nm 100 fs laser pulse. Due to the large moment of inertia along the C-I axis and the small anisotropic dipole polarizability of  $\text{CH}_3\text{I}$  it is that the anisotropic angular distributions resulting from CE of the fragment ions are due to geometric alignment [51], as was also concluded in previous studies of polyatomic molecules, such as  $\text{CS}_2$  [25],  $\text{C}_2\text{H}_5\text{OH}$  [52],  $\text{C}_2\text{H}_4$  [53] and  $\text{CH}_2\text{I}_2$  [54]. The angular distribution in the recoil velocity of the  $I^{q+}$  fragments of the Coulomb exploded  $\text{CH}_3\text{I}$  is expected to be partial due to PIA as discussed in Section 3.5.

It is interesting to note that for the  $\text{CH}_3\text{I}$  explosion channels the angular distribution of the  $I^+$  ion fragment  $G_1(2, 1)$  channel is remarkable similar to that of the  $G_2(1, 2)$  channel  $I^{2+}$  ion fragment. This in spite of their not identical KERs energies:  $0.65 \pm 0.02$  eV for the  $G_1(2, 1)$  component and  $0.80 \pm 0.07$  eV for the  $G_2(1, 2)$  component. A similar resemblance was found for the angular distribution of the  $I^{2+}$  component  $G_2(3, 2)$  of the  $I^{2+}$  and the  $G_3(2, 3)$  component of  $I^{3+}$ . The same angular distributions and kinetic energies indicate that these components of different ions are produced from the same precursor ions via Coulomb Explosion.

## 4 Conclusion

In this work, we have investigated dissociative ionization and coulomb explosion of  $\text{CH}_3\text{I}$  induced by femtosecond laser at 800 nm using a velocity map ion imaging method. KERs and angular distributions of fragment ions were measured and accordingly the different dissociative ionization and coulomb explosion channels have been identified. By investigating the angular distribution of the fragment ions  $I^{n+}$  ( $n = 1-3$ ) at laser intensities ranging from about  $3 \times 10^{14}$  to  $6 \times 10^{14}$  W/cm<sup>2</sup>, geometric alignment was concluded to be mainly responsible for the observed anisotropy. Geometrical ionization and PIA enhanced ionization schemes have applied to interpret the experimental observation that the measured kinetic energies for  $I^{n+}$  ( $n = 1-3$ ) increase and sharpen with increasing laser intensity for the  $\text{CH}_3\text{I}$  Coulomb explosion channels.

This work was supported by the National Natural Science Foundation of China.

## Author contribution statement

D.D.Z. and S.Z.L. performed the experiments and analysed the data. D.D.Z., W.R. and S.S. wrote the manuscript. A.E. provided the software for reconstruct the images. H.L. and D.W.J. provided the electronics support for the experiments. B.Y. and Z.G.W. provided the theoretical calculation of the energy level of the charged  $\text{CH}_3\text{I}$  molecule. D.D.Z., S.Z.L., H.F.X., F.C.L., M.X.J. and D.J.D. took part in discussions on the analyses of the data. D.D.Z., H.F.X., W.R., S.S. and D.J.D. took part in discussions on the content of the manuscript. D.J.D. supervised the project.

**Open Access** This is an open access article distributed under the terms of the Creative Commons Attribution License (<http://creativecommons.org/licenses/by/4.0>), which permits unrestricted use, distribution, and reproduction in any medium, provided the original work is properly cited.

## References

- K. Codling, L.J. Frasinski, *J. Phys. B: At. Mol. Opt. Phys.* **26**, 783 (1993)
- P.B. Corkum, P. Dietrich, *Comm. At. Mol. Phys.* **28**, 357 (1993)
- A. Giusti-Suzor, F.H. Mies, L.F. DiMauro, E. Charron, B. Yang, *J. Phys. B: At. Mol. Opt. Phys.* **28**, 309 (1995)
- F.A. Ilkov, T.D.G. Walsh, S. Turgeon, S.L. Chin, *Phys. Rev. A* **51**, R2695 (1995)
- M.J. DeWitt, R.J. Levis, *Phys. Rev. Lett.* **81**, 5101 (1998)
- C. Wu, Y. Xiong, N. Ji, Y. He, Z. Gao, F.A. Kong, *J. Phys. Chem. A* **105**, 374 (2000)
- C. Ellert, H. Stapelfeldt, E. Constant, H. Sakai, J. Wright, D.M. Rayner, P.B. Corkum, *Philos. Trans. Roy. Soc. London, Ser. A: Math. Phys. Eng. Sci.* **356**, 329 (1998)
- A. Iwamae, A. Hishikawa, K. Yamanouchi, *J. Phys. B: At. Mol. Opt. Phys.* **33**, 223 (2000)
- S. Chelkowski, A.D. Bandrauk, *J. Phys. B: At. Mol. Opt. Phys.* **28**, L723 (1995)
- K.W.D. Ledingham, D.J. Smith, R.P. Singhal, T. McCanny, P. Graham, H.S. Kilic, W.X. Peng, A.J. Langley, P.F. Taday, C. Kosmidis, *J. Phys. Chem. A* **103**, 2952 (1999)
- G.L. Kamta, A.D. Bandrauk, *Phys. Rev. Lett.* **94**, 203003 (2005)
- X.-P. Tang, S.-F. Wang, M.E. Elshakre, L.-R. Gao, Y.-I. Wang, H.F. Wang, F.-I. Kong, *J. Phys. Chem. A* **107**, 13 (2003)
- S. Wang, X. Tang, L. Gao, M.E. Elshakre, F. Kong, *J. Chem. Phys. A* **107**, 6123 (2003)
- M.E. Elshakre, L. Gao, X. Tang, S. Wang, Y. Shu, F. Kong, *J. Chem. Phys.* **119**, 5397 (2003)
- D. Pavičić, A. Kiess, T.W. Hänsch, H. Figger, *Phys. Rev. Lett.* **94**, 16300 (2005)
- T. Seideman, M.Y. Ivanov, P.B. Corkum, *Phys. Rev. Lett.* **75**, 2819 (1995)
- M. Brewczyk, L.J. Frasinski, *J. Phys. B: At. Mol. Opt. Phys.* **24**, L307 (1991)
- J.H. Posthumus, L.J. Frasinski, A.J. Giles, K. Codling, *J. Phys. B: At. Mol. Opt. Phys.* **28**, L349 (1995)
- A.D. Bandrauk, H.Z. Lu, *Phys. Rev. A* **62**, 053406 (2000)
- G.L. Kamta, A.D. Bandrauk, *Phys. Rev. A* **70**, 011404 (2004)
- H. Sabzyan, M. Vafaei, *Phys. Rev. A* **71**, 063404 (2005)
- X. Tong, Z. Zhao, C. Lin, *Phys. Rev. A* **66**, 033402 (2002)
- X.M. Tong, Z.X. Zhao, A.S. Alnaser, S. Voss, C.L. Cocke, C.D. Lin, *J. Phys. B: At. Mol. Opt. Phys.* **38**, 333 (2005)
- C. Wu, Y. Yang, Z. Wu, B. Chen, H. Dong, X. Liu, Y. Deng, H. Liu, Y. Liu, Q. Gong, *Phys. Chem. Chem. Phys.* **13**, 18398 (2011)
- P. Graham, K.W.D. Ledingham, R.P. Singhal, T. McCanny, S.M. Hankin, X. Fang, D.J. Smith, C. Kosmidis, P. Tzallas, A.J. Langley, P.F. Taday, *J. Phys. B: At. Mol. Opt. Phys.* **32**, 5557 (1999)
- F. Rosca-Pruna, E. Springate, H.L. Offerhaus, M. Krishnamurthy, N. Farid, C. Nicole, M.J.J. Vrakking, *J. Phys. B: At. Mol. Opt. Phys.* **34**, 4919 (2001)
- E. Springate, F. Rosca-Pruna, H.L. Offerhaus, M. Krishnamurthy, M.J.J. Vrakking, *J. Phys. B: At. Mol. Opt. Phys.* **34**, 4939 (2001)
- M. Schmidt, S. Dobosz, P. Meynadier, P. D'Oliveira, D. Normand, E. Charron, A. Suzor-Weiner, *Phys. Rev. A* **60**, 4706 (1999)
- J.H. Posthumus, J. Plumridge, M.K. Thomas, K. Codling, L.J. Frasinski, A.J. Langley, P.F. Taday, *J. Phys. B: At. Mol. Opt. Phys.* **31**, L553 (1998)
- J.H. Posthumus, A.J. Giles, M.R. Thompson, K. Codling, *J. Phys. B: At. Mol. Opt. Phys.* **29**, L525 (1996)
- P. Graham, K.W.D. Ledingham, R.P. Singhal, T. McCanny, S.M. Hankin, X. Fang, P. Tzallas, C. Kosmidis, P.F. Taday, A.J. Langley, *J. Phys. B: At. Mol. Opt. Phys.* **33**, 3779 (2000)
- S. Couris, E. Koudoumas, S. Leach, C. Fotakis, *J. Phys. B: At. Mol. Opt. Phys.* **32**, L439 (1999)
- A.T.J.B. Eppink, D.H. Parker, *J. Chem. Phys.* **109**, 4758 (1998)
- Y.-J. Jung, Y.S. Kim, W.K. Kang, K.-H. Jung, *J. Chem. Phys.* **107**, 718 (1997)
- A.J. van den Brom, M. Laura Lipciuc, M.H.M. Janssen, *Chem. Phys. Lett.* **368**, 324 (2003)
- P.C. Samartzis, B.L.G. Bakker, D.H. Parker, T.N. Kitsopoulos, *J. Phys. Chem. A* **103**, 6106 (1999)
- J.J. Larsen, H. Sakai, C.P. Safvan, I. Wendt-Larsen, H. Stapelfeldt, *J. Chem. Phys.* **111**, 7774 (1999)
- A. Sugita, M. Mashino, M. Kawasaki, Y. Matsumi, R.J. Gordon, R. Bersohn, *J. Chem. Phys.* **112**, 2164 (2000)
- P. Graham, K.W.D. Ledingham, R.P. Singhal, S.M. Hankin, T. McCanny, X. Fang, C. Kosmidis, P. Tzallas, P.F. Taday, A.J. Langley, *J. Phys. B: At. Mol. Opt. Phys.* **34**, 4015 (2001)
- R. Ma, C. Wu, N. Xu, J. Huang, H. Yang, Q. Gong, *Chem. Phys. Lett.* **415**, 58 (2005)
- H. Liu, Z. Yang, Z. Gao, Z. Tang, *J. Chem. Phys.* **126**, 044316 (2007)
- Y. Wang, S. Zhang, Z. Wei, B. Zhang, *J. Phys. Chem. A* **112**, 3846 (2008)
- M.E. Corrales, G. Gitzinger, J. González-Vázquez, V. Lorient, R. de Nalda, L. Bañares, *J. Phys. Chem. A* **116**, 2669 (2012)
- A.T.J.B. Eppink, D.H. Parker, *Rev. Sci. Instrum.* **68**, 3477 (1997)
- M. Lee, M.S. Kim, *J. Chem. Phys.* **127**, 124313 (2007)
- L.V. Keldysh, *Sov. Phys. JETP* **20**, 1307 (1965)
- P. Sharma, R.K. Vatsa, B.N. Rajasekhar, N.C. Das, T.K. Ghanty, S.K. Kulshreshtha, *Rapid Commun. Mass Sp.* **19**, 1522 (2005)
- K. Walter, R. Weinkauff, U. Boesl, E.W. Schlag, *J. Chem. Phys.* **89**, 1914 (1988)
- Y.J. Bae, M.S. Kim, *J. Chem. Phys.* **128**, 124324 (2008)
- S. Pratt, *Phys. Rev. A* **33**, 1718 (1986)
- H. Stapelfeldt, T. Seideman, *Rev. Mod. Phys.* **75**, 543 (2003)
- J. Chen, R. Ma, H. Ren, X. Li, H. Yang, Q. Gong, *Int. J. Mass Spectrom.* **241**, 25 (2005)
- M. Castillejo, M. Martin, R. de Nalda, S. Couris, E. Koudoumas, *J. Chem. Phys. A* **106**, 2838 (2002)
- X. Zhang, D. Zhang, H. Liu, H. Liu, H. Xu, M. Jin, D. Ding, *J. Phys. B: At. Mol. Opt. Phys.* **43**, 025102 (2010)